### Title

Vortex simulations on a 3-sphere




### Journal

Physical Review Research, 1(3)

### ISSN

2643-1564



### Authors

Dix, OM

Zieve, RJ



### Publication Date

2019-12-01

### DOI

10.1103/physrevresearch.1.033201

Peer reviewed

# Vortex Simulations on a 3-Sphere

O.M. Dix and R.J. Zieve
*Physics Department, University of California at Davis*

We generate vortex tangles using a Hopf flow on a 3-sphere, in place of the standard torus defined by periodic boundary conditions. These tangles are highly anisotropic, with vortices tending to align along the flow direction. Standard power law dependences change accordingly from their values in more isotropic tangles. The line length density $\langle L\rangle$ is proportional to $v_{ns}^{1.28}$, where $v_{ns}$ is the drive velocity, and the reconnection rate depends roughly on $\langle L\rangle^2$. We also discuss the effect of the full Biot-Savart law versus the local induction approximation (LIA). Under LIA the tangle collapses so that all vortices are nearly aligned with a single flow line, in sharp contrast to the torus where they become perpendicular to the driving velocity. Finally we present a few torus simulations with a helical velocity field, which in some ways resembles the 3-sphere flow.

## I. INTRODUCTION

The notoriously intractable equations governing fluid flow generate a great deal of numerical work [1–4]. While many calculations deal directly with the velocity field, others focus on the vorticity [4]. The latter is natural for a variety of flows with intense vorticity, including airplane trailing vortices, severe weather events such as hurricanes and tornadoes, and the molecular clouds that lead to star formation. Vortex methods track the positions of vortex filaments over time, by calculating the velocity field from the vortex locations and then using it to update the vortices. Such calculations are particularly well-suited to superfluid helium, where the restriction of vorticity to angstrom-scale cores makes the "slender filament" approximation quite accurate, and a great deal of work has been devoted to understanding such simulations of superfluid vortices [5, 6].

Efforts to identify general principles necessarily focus on idealized cases, such as homogeneous turbulence. Since homogeneity is destroyed near a boundary, computations can take two approaches. One is to use a large, finite volume, but to evaluate properties only in a smaller region far from the boundaries. The other is to run calculations in a space without boundaries. The latter has several advantages, notably that there is no need to deal with the complex behavior at surfaces, and that the entire computational power can be devoted to the region of interest. The standard choice is periodic boundary conditions. Topologically, these three-dimensional simulations run on the three-dimensional torus $T^3$ rather than in infinite $\mathbb{R}^3$.

The choice of periodic boundary conditions can affect the calculation results. An example encountered in vortex filament simulations is the tendency of vortices to fall into an "open-orbit" state, where they align parallel to each other and perpendicular to the driving velocity field [7, 8]. In this configuration they interact only trivially with the velocity field, resulting in uniform translation of the entire set of vortices, so the open-orbit state persists indefinitely. Since this state requires the vortices to be closed loops that are perpendicular to the velocity field everywhere, it corresponds to a set of infinite straight vortex lines in $\mathbb{R}^3$. Vortex rings in $\mathbb{R}^3$, unlike those in $T^3$, cannot exhibit such behavior. The particular case of the open-orbit state can be prevented by including non-local interaction terms between vortices in addition to the Arms-Hama local term [9], but it nevertheless demonstrates the possibility of topological artifacts. This raises the question of how else the topology may affect simulation results.

Here we present vortex filament simulations in a different three-dimensional space, namely a 3-sphere $S^3$, the surface of a four-dimensional ball. We find several unusual behaviors, including a tendency for vortices to align with the velocity flow instead of perpendicular to it. A particularly interesting result is the unusually high degree of directionality in homogeneous vortex tangles, which provides a testing ground for predictions about anisotropic turbulence.

## II. COMPUTATIONAL CONSIDERATIONS

As is standard in vortex filament simulations [5, 10], we consider a vortex line $\mathbf{s}(\xi,t)$, where $\xi$ is arc length and $t$ is time. The vortex moves according to

$$\dot{\mathbf{s}} = \dot{\mathbf{s}}_0 + \alpha \mathbf{s}' \times (\mathbf{v}_n - \dot{\mathbf{s}}_0). \tag{1}$$

Here $\mathbf{s}' = d\mathbf{s}/d\xi$ is the unit tangent to the vortex, $\mathbf{v}_n$ is the applied normal fluid velocity that supplies energy to the vortex tangle, and $\alpha$ is a coefficient of mutual friction between the normal and superfluid components. We take $\alpha = 0.1$, corresponding to a temperature of about 1.6 K in superfluid $^4$He. The complete version of Equation 1 includes an additional mutual friction term $-\alpha' \mathbf{s}' \times (\mathbf{s}' \times (\mathbf{v}_{ns} - \dot{\mathbf{s}}_0))$, but as is often done in helium vortex simulations we set the coefficient $\alpha' = 0$ and neglect this contribution. Finally, $\dot{\mathbf{s}}_0$ is the local superfluid velocity, given by the Biot-Savart law. In $\mathbb{R}^3$ this is

$$\dot{\mathbf{s}}_0 = \frac{\kappa}{4\pi} \int_{\mathscr{L}} \frac{(\mathbf{s}_1 - \mathbf{s}) \times d\mathbf{s}_1}{|\mathbf{s}_1 - \mathbf{s}|^3},$$

where $\kappa$ is the circulation quantum and the integral is over all the vortex lines. We will discuss below the modifications needed to this integral for use in $S^3$.

For numerical evaluation, the vortex is approximated by a sequence of points with straight line segments connecting neighboring points. In evaluating the velocity at $\mathbf{s}$, the two vortex segments adjacent to $\mathbf{s}$ must be removed from the integral. They are replaced by a term proportional to the local curvature of the vortex line, which is scaled to agree with the analytically calculated velocity for circular vortex rings. The

expression for local superfluid velocity becomes

$$\dot{\mathbf{s}}_0 = \beta \mathbf{s}' \times \mathbf{s}'' + \frac{\kappa}{4\pi} \int_{\mathscr{L}}' \frac{(\mathbf{s}_1 - \mathbf{s}) \times d\mathbf{s}_1}{|\mathbf{s}_1 - \mathbf{s}|^3},$$

where $\mathbf{s}'' = d^2\mathbf{s}/d\xi^2$ is the curvature vector. The prefactor $\beta$ is set to

$$\beta = \frac{\kappa}{4\pi} \ln\left(\frac{2\sqrt{\ell_+ \ell_-}}{e^{1/4} a_0}\right),$$

which yields the correct behavior for circular vortex loops in $\mathbb{R}^3$ with uniform point spacing. $a_0$ is the core radius of a vortex filament, and $\ell_\pm$ are the distances between the point where the velocity is being calculated and its neighbors on each side. Our calculations use values appropriate to superfluid $^4$He, $\kappa = 9.969 \times 10^{-4}$ cm$^2$/s and $a_0 = 1.3 \times 10^{-8}$ cm.

We use a 3-sphere embedded in $\mathbb{R}^4$, consisting of points $(x, y, z, w)$ such that $x^2 + y^2 + z^2 + w^2 = R^2$. (Mathematicians often use $S^3$ for the sphere of unit radius, but we will use this notation more generally for our sphere of radius $R$.) Four-dimensional Cartesian coordinates help with much of the necessary calculation. For the driving velocity, we use a Hopf vector field, given in $\mathbb{R}^4$ as $\mathbf{v} = \frac{v}{R}(-y, x, -w, z)$. This Hopf velocity field possesses several useful properties. It is tangent to $S^3$, so it drives vortex motion entirely within the manifold. It also has uniform magnitude $v$ and zero divergence. However, it is not irrotational; in fact its curl in $S^3$ is $\frac{2}{R}\mathbf{v}$, parallel to the Hopf field itself [11]. We assign the driving Hopf velocity field to the normal fluid, which unlike the superfluid is not required to be irrotational. Nonetheless, as we shall see, the non-zero curl has consequences for the vortex behavior.

Several adjustments are needed when restricting to $S^3$. To begin with, distances such as $|\mathbf{s}_1 - \mathbf{s}|$ should be calculated along the geodesic through the two points, rather than along the shorter chord that connects the points in $\mathbb{R}^4$. Next, vectors defined at a point on $S^3$ lie in the tangent space of $S^3$ at that point. Vector operations such as dot products or cross products can be performed within a tangent space. However, in our calculations relevant vectors are often defined at two different points of $S^3$, where the tangent spaces themselves differ. Viewed as a vector within $\mathbb{R}^4$, one vector may not even be in the tangent space where the other vector is defined. For vectors in different tangent spaces, we parallel transport one vector along a geodesic to the location of the other vector, before carrying out any further vector operations [12]. Once we are working with two vectors in the same tangent space, the dot product takes exactly its value in $\mathbb{R}^4$. For cross-products in the tangent space at $\mathbf{q}$, we use the determinant of a $4 \times 4$ matrix:

$$\text{cross}(\mathbf{v_1}, \mathbf{v_2}, \mathbf{q}) \cdot \mathbf{a} = \frac{1}{R} \begin{vmatrix} v_{1x} & v_{1y} & v_{1z} & v_{1w} \\ v_{2x} & v_{2y} & v_{2z} & v_{2w} \\ q_x & q_y & q_z & q_w \\ a_x & a_y & a_z & a_w \end{vmatrix}$$

Here $\mathbf{a}$ is an arbitrary vector in $\mathbf{R}^4$; taking it to be a unit vector selects the component of the cross-produce in that direction. Given three vectors $\mathbf{v_1}$, $\mathbf{v_2}$, and $\mathbf{q}/R$, the cross-product is a vector orthogonal to all three and with magnitude defined by the volume of the parallelopiped spanned by the three vectors. Since $\mathbf{q}$ is the normal vector to the 3-sphere, the cross-product must lie in the tangent space at $\mathbf{q}$.

Some of the vectors involved in the calculations, particularly the curvature vectors of vortex lines as calculated in $\mathbb{R}^4$, may have components along the 3-sphere radius vector. Such radial components give no contribute to cross-products, but they could affect dot products. We explicitly remove any radial component of a vector before proceeding with further operations. In the case of curvature vectors, this has the effect of removing the intrinsic curvature of the 3-sphere from our calculations.

Another issue is that numerical evaluation of Equation 1 yields a velocity vector in a tangent space to $S^3$, not in $S^3$ itself. Using such velocity vectors to update the locations of vortex core would result in new locations outside the 3-sphere. Projecting these points directly back to the 3-sphere would slightly decrease the distance traveled during the time step. Instead, we move the vortex points by the desired distance but along the geodesic defined by the projection of the velocity onto $S^3$.

The Biot-Savart law must also be treated differently on $S^3$ from on $T^3$. The torus has no curvature, so within regions very small compared to the torus diameters, the Biot-Savart expression of $\mathbb{R}^3$ can be used. As the distance between the vortex segment and the test point grows, additional contributions enter corresponding to paths that loop around the torus, as shown in Figure 1 for $T^2$. The shortest path between any part of the vortex and the point indicated lies near the dotted line 1; in the analogous three-dimensional situation, this would give certain Biot-Savart contributions to the velocity field at the test point. On the other hand, the dotted line 2 corresponds to paths not much longer but in an entirely different direction, which would give very different contributions. Other paths, wrapping around the torus one or more times, are also possible. The multiple contributions have sometimes been accounted for by representing the torus as a periodic cube tiling $\mathbb{R}^3$, and adding contributions from the original vortex segment and also from its images, out to some distance beyond which further contributions are deemed negligible [13].

On $S^3$ the standard Cartesian Biot-Savart expression is again merely an approximate solution, both because alternate paths may traverse the sphere in different directions and because the curvature of the sphere makes the resemblance to $\mathbb{R}^3$ only local. Some of our computations use the standard Euclidean Biot-Savart law within a limited region of $S^3$. To update the position of a point $P$ along the vortex core, we need to calculate the fluid velocity at that point. We use parallel transport to map all vectors needed for the calculation into the tangent space at $P$. We then carry out the calculation within that tangent space. We calculate contributions only from vortex segments sufficiently close to $P$.

Most of our calculations use a different approach. Unlike on $T^3$, there exists an exact form for the Biot-Savart law on $S^3$ [14, 15], which allows a more complete calculation of the velocity field produced by vortex segments. We generally use the full 3-sphere Biot-Savart law. We retain contributions to velocity either from vortices on the entire sphere,

or from those in a limited region surrounding the evaluation point. Whether we use the Cartesian Biot-Savart law or the exact expression on $S^3$, we project the calculated velocity vector onto a geodesic and move $P$ an appropriate distance along that geodesic.

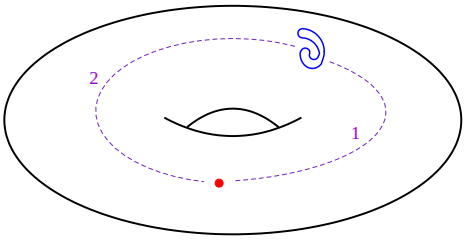


FIG. 1: Two possible paths from a vortex loop (blue online) to the same point (red online) on a torus.

We follow the presentation by DeTurck and Gluck of the Biot-Savart law on the 3-sphere [14]. The contribution to the velocity field at a point $\mathbf{q}$ from a vortex line $U$ on $S^3$ is given by

$$d\mathbf{v} = \int_U \nabla_q \phi(u,q) \times P_{qu} d\mathbf{u}. \tag{2}$$

Here $P_{qu}$ is the parallel transport operation described above, which takes a vector from the tangent space at $\mathbf{u}$ to the tangent space at $\mathbf{q}$. The function $\phi$ depends only on the distance $h = |\mathbf{q}-\mathbf{u}|$ along the geodesic connecting its two arguments and has the form

$$\phi(h) = \frac{\kappa}{4\pi^2 R^2}\left(\pi - \frac{h}{R}\right)\csc\frac{h}{R}. \tag{3}$$

The familiar Biot-Savart law in $\mathbb{R}^3$ would instead use $\phi(h) = \kappa/4\pi h$, with $h$ the distance along the straight-line path from $\mathbf{q}$ to $\mathbf{u}$.

For the Biot-Savart calculation we consider the vortex core as a series of points connected by straight segments, i.e. geodesics. We evaluate the integral of Equation 2 exactly along each of these finite-length geodesic segments, as shown in Figure 2. In the integrand, $\nabla\phi$ is calculated in the tangent space at $\mathbf{q}$. Since $\phi$ depends only on the separation between the points $\mathbf{u}$ and $\mathbf{q}$, the gradient must be in the direction where this separation changes the fastest, which is the direction of the geodesic containing the two points. We use

$$\nabla_q \phi = \frac{\partial \phi}{\partial h}\nabla_q h$$

and observe that $\nabla_q h$ has magnitude 1 and is directed away from $\mathbf{u}$ along the geodesic connecting $\mathbf{u}$ and $\mathbf{q}$.

Next consider the effect of parallel transport along this geodesic. The geodesic lies in a plane of $\mathbb{R}^4$, defined by the tangent to the geodesic and the normal to the 3-sphere at any point on the geodesic, such as $\mathbf{u}$. Parallel transport of any vector rotates the vector within this plane, without affecting the components orthogonal to the plane. This has two implications for the calculation at hand. First, no parallel transport

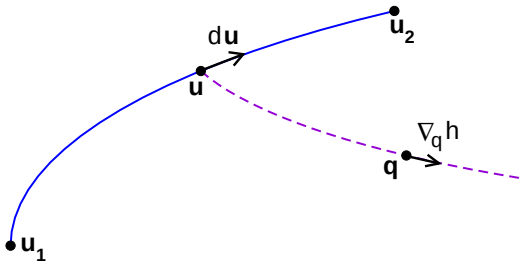


FIG. 2: Integration along a geodesic (solid curve), to evaluate Biot-Savart contribution at point $\mathbf{q}$. The dashed curve is the geodesic between $\mathbf{q}$ and a point $\mathbf{u}$ on the integration path.

calculation is necessary for the integral of Equation 2. Only the components of $P_{qu}d\mathbf{u}$ within the tangent space but perpendicular to the geodesic contribute to the cross-product in the integrand, and these are exactly the components unchanged by parallel transport. Second, we can use $\mathbf{u}$ to construct a unit vector along the geodesic. The plane of a geodesic contains the normal vectors to $S^3$ at every point on that geodesic, so $\mathbf{u}$ can be decomposed into one component along $\mathbf{q}$ and another tangent to the geodesic at $\mathbf{q}$. Its projection into the tangent space at $\mathbf{q}$ is this latter component. Since the angle between $\mathbf{u}$ and $\mathbf{q}$ is $h/R$, the two components have magnitude $R\cos\frac{h}{R}$ and $R\sin\frac{h}{R}$. Rescaling, the projection of $-\frac{1}{\sin(h/R)}\hat{\mathbf{u}}$ into the tangent space at $\mathbf{q}$ is a unit vector along the geodesic, directed away from $\mathbf{u}$. For Equation 2 we can use $-\frac{1}{\sin(h/R)}\hat{\mathbf{u}}$ rather than $\nabla_q h$; although these vectors are not identical, the component of the former perpendicular to the tangent space does not contribute to the cross-product. Using this fact and explicitly calculating $\partial\phi/\partial h$, Equation 2 becomes

$$d\mathbf{v} = \frac{\kappa}{4\pi^2 R^2}\int_{\mathbf{u}_1}^{\mathbf{u}_2} d\mathbf{u}\times\hat{\mathbf{u}}\frac{\sin\frac{h}{R} + (\pi - \frac{h}{R})\cos\frac{h}{R}}{\sin^3\frac{h}{R}}.$$

Up to this point the discussion does not depend on the shape of the integration path from $\mathbf{u}_1$ to $\mathbf{u}_2$. We now take that path to be a geodesic. This is distinct from the geodesic of the previous paragraph, which goes from the test point to the integration path. Next we set coordinates for evaluating the integral. The geodesic integration path defines a plane in $\mathbb{R}^4$, which we take as the $xy$-plane. We take the projections of $\mathbf{q}$ within and perpendicular to the $xy$-plane to lie along the positive $x$ and $z$ axes, respectively. Thus $\mathbf{u} = R(\cos\theta, \sin\theta, 0, 0)$, with $\theta_1$ and $\theta_2$ denoting the integration limits, and $\mathbf{q} = R(\cos\psi, 0, \sin\psi, 0)$, where $0 \le \psi \le \pi/2$. Hence $d\mathbf{u} = R(-\sin\theta, \cos\theta, 0, 0)d\theta$ and the integral becomes

$$d\mathbf{v} = -\frac{\kappa}{4\pi^2}\hat{\mathbf{w}}\int_{\theta_1}^{\theta_2} d\theta \sin\psi\frac{\sin\frac{h}{R} + (\pi - \frac{h}{R})\cos\frac{h}{R}}{\sin^3\frac{h}{R}},$$

where $h$ depends on $\theta$. We can also adjust the integral so that $\sin\theta \ge 0$, as follows. If the original choice of coordinates gives $\sin\theta \le 0$ along the entire geodesic, then rotation by $\pi$ in the $yw$-plane switches the geodesic segment to positive $\theta$ without altering $\mathbf{q}$. If $\sin\theta$ changes sign along the geodesic,

then the curve can be divided into two segments and the calculation carried out separately for the two. The geodesic segments we integrate along connect consecutive points on a vortex core and are always too short for $\sin\theta$ to change sign more than once.

The variables $\theta$, $\psi$, and $h$ are related through

$$\cos\frac{h}{R} = \frac{\mathbf{u}\cdot\mathbf{q}}{R^2} = \cos\theta\cos\psi.$$

Using $-\frac{1}{R}\sin\frac{h}{R}dh = -\sin\theta\cos\psi d\theta$ and assuming $\sin\theta \geq 0$, we have

$$d\mathbf{v} = -\frac{\kappa\sin\psi}{4\pi^2 R}\hat{\mathbf{w}}\int_{h_1}^{h_2} dh \frac{\sin\frac{h}{R} + (\pi - \frac{h}{R})\cos\frac{h}{R}}{\sin^2\frac{h}{R}\sqrt{\cos^2\psi - \cos^2\frac{h}{R}}}.$$

An additional minus sign would appear if $\sin\theta\cos\psi < 0$, but our choice of coordinates ensures that this is not the case. Integrating gives

$$d\mathbf{v} = \hat{\mathbf{w}}\frac{\kappa\sin\psi}{4\pi^2(\cos^2\psi - 1)}\left(-\arcsin\left(\frac{\cos\frac{h}{R}}{\cos\psi}\right)\right.$$

$$\left. + \frac{(\pi - \frac{h}{R})\sqrt{\cos^2\psi - \cos^2\frac{h}{R}}}{\sin\frac{h}{R}}\right)\Bigg|_{h_1}^{h_2}$$

where our coordinates again eliminate any ambiguity in the sign of the first term. In the coordinates used above for the geodesic segment, the contribution is always in the **w** direction. We then rotate it back into the original coordinate frame in which the vortices are defined, repeat for each geodesic segment along the vortices, and add the results to obtain the Biot-Savart integral along the entire set of vortices.

## III. PROPERTIES OF STABLE TANGLES

Calculations using these equations successfully produce vortex tangles, as shown in Figure 3. We use two types of projection, Hopf and stereographic, to display the vortex configuration. These are described in more detail in the appendix, as well as in algebraic topology textbooks [16]. The right column of Figure 3 uses stereographic projection, which maps $S^3$ onto flat three-dimensional space $\mathbb{R}^3$. One point of $S^3$ goes to infinity, and its antipode maps to the origin. A sphere within $S^3$, centered at either of these points, maps to a sphere in $\mathbb{R}^3$ centered at the origin. Hence the half of $S^3$ closest to the point sent to the origin maps to a ball centered at the origin. The other half of $S^3$ maps to the remainder of $\mathbb{R}^3$ outside of the ball. Some portions of the vortex lines in Figure 3 lie outside the displayed region. The second type of visualization, shown in the left column of Figure 3, is the Hopf projection, which maps $S^3$ onto $S^2$, the two-dimensional surface of a ball in $\mathbb{R}^3$. Each Hopf fiber maps to a single point of $S^2$. This mapping is particularly informative when vortices align closely with the velocity field, since after projection such vortices appear as points or very small loops.

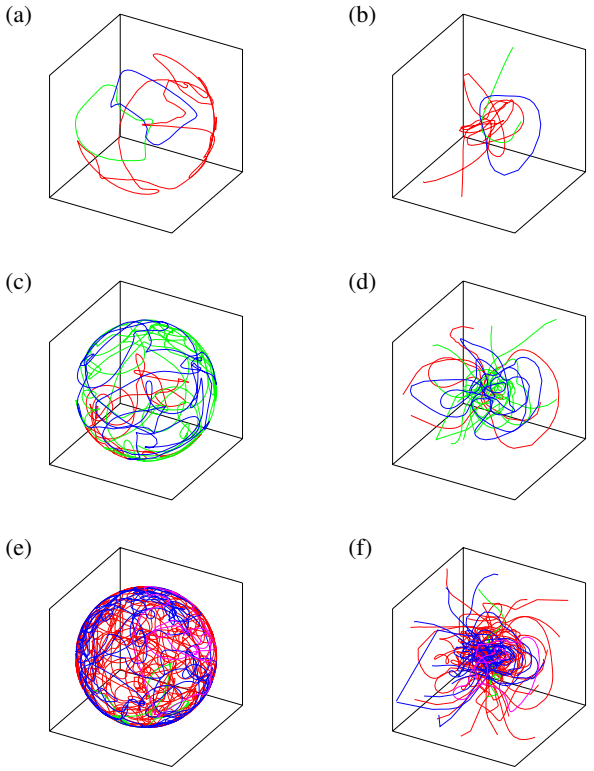


FIG. 3: Hopf and stereographic projections of vortex tangles for $v_{ns}$ = 1, 2, 4 cm/s.

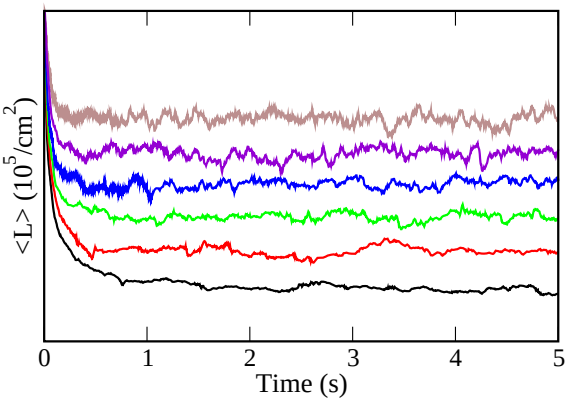


FIG. 4: Line length density as a function of time, for (bottom to top) $v_{ns}$ = 1, 1.2, 1.4, 1.6. 1.8, 2 cm/s.

As seen previously in many calculations using periodic boundary conditions [7–9, 13, 17, 18], the vortex tangle eventually reaches a steady state where various statistical properties remain constant over time. Figure 4 shows the time development of the average vortex line density, for several different driving velocities. The flat portion of each curve corresponds to the steady-state situation. As the driving velocity $v_{ns}$ increases, the line density increases monotonically and the time to reach the steady-state density decreases.

We find that the statistical behavior of tangles is independent of the initial conditions for the calculations, as shown in Figure 5. Furthermore, the more familiar, approximate Biot-Savart calculation provides confirmation that the exact formula functions correctly. The two agree well for dynamics of simple vortex configurations, such as a single circular vortex ring. Their results for line length density and tangle anisotropy also agree, not only for very short-distance calculations of vortex interactions, where the approximation should be quite good, but even when applied on as much as a full hemisphere. Thus Figure 5 shows that line length density equilibrates at the same level for three simulations with different initial conditions, two using the exact Biot-Savart law and the third using the approximate version. In each case vortex interactions out to a hemisphere were included. We do not attempt to use the approximate Biot-Savart law at larger distances.

Despite the rapid achievement of a steady-state line density in Figure 4, the tangles, particularly for low $v_{ns}$, are not entirely homogeneous. Figure 6 shows the line density in four of the sixteen orthants of $S^3$. Although the line density is very similar in certain pairs of orthants, in others it differs significantly. We number the orthants by assigning one bit to each of the four Cartesian coordinates of the space $\mathbb{R}^4$ that contains the 3-sphere. A negative coordinate corresponds to a bit value of zero, and a positive or zero coordinate to a value of one. We place the $x$ bit in the rightmost position, then the $y$ bit, then $z$, and finally the $w$ bit in the leftmost position. Thus orthant 1 has $x \geq 0$, $y < 0$, $z < 0$, and $w < 0$, while orthant 13 has $x \geq 0$, $y < 0$, $z \geq 0$, and $w \geq 0$. As Figure 7 shows, the line densities in certain pairs of orthants continue to diverge for several seconds, even though the long-time average line density is the same in both orthants. The issue is not a slow approach to the steady state line density, but rather slow communication between different regions of $S^3$ even in the steady state.

The top frame of Figure 8 shows the line length density for all sixteen orthants, averaged over the same four seconds of steady-state tangle shown in Figure 6. The orthants separate into four groups by line density. Orthants 0, 5, 10, and 15 have by far the largest line density. The next group is orthants 1, 7, 8, and 14; then orthants 2, 4, 11, and 13 with nearly identical line length densities; and finally orthants 3, 6, 9, and

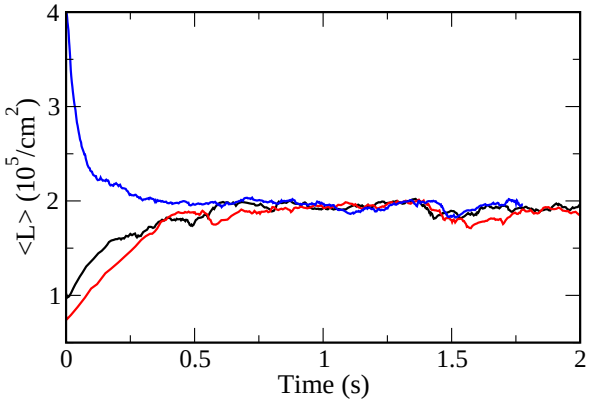


FIG. 5: Line length density $\langle L \rangle$ as a function of time, for $v_{ns} = 1.4$ cm/s and non-local interactions calculated within a hemisphere, for three different initial configurations. The two calculations with initially increasing $\langle L \rangle$ use the exact Biot-Savart law, while the third uses the approximate Biot-Savart formula.

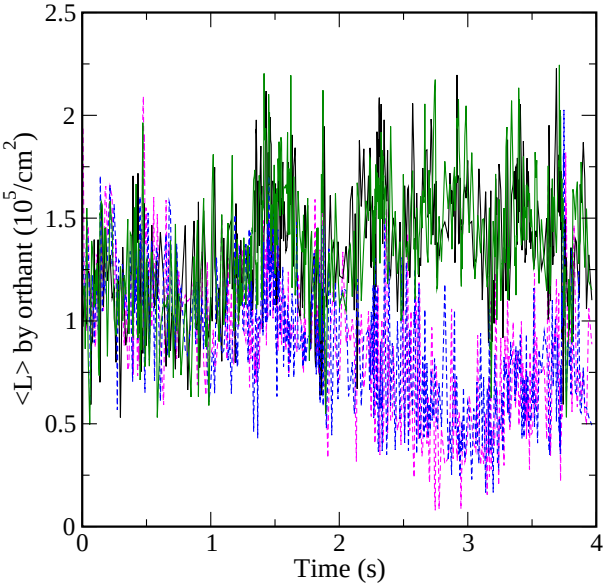


FIG. 6: Line length density as a function of time for $v_{ns}$ = 1 cm/s, for orthants 9 (magenta, dashed), 10 (black, solid), 12 (blue, dashed), and 15 (green, solid). The two solid curves track each other closely, as do the two dashed curves, showing rapid homogenization in the corresponding orthants.

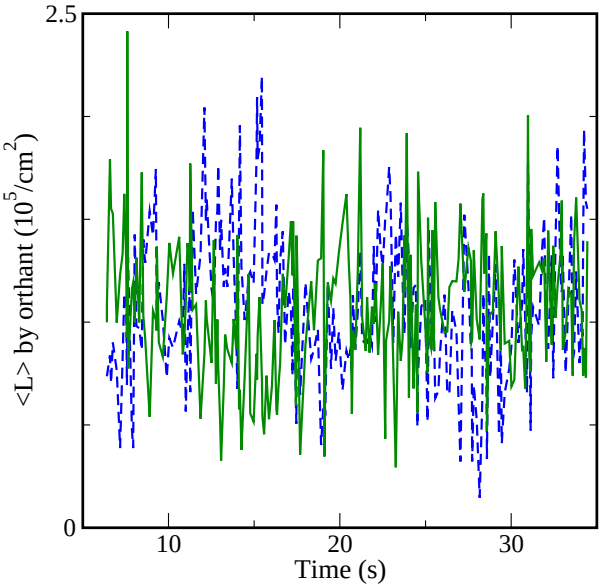


FIG. 7: Continuation of line length density from Figure 6, for orthants 12 (blue, dashed) and 15 (green, solid). Over sufficiently long times the average density is the same in each orthant.

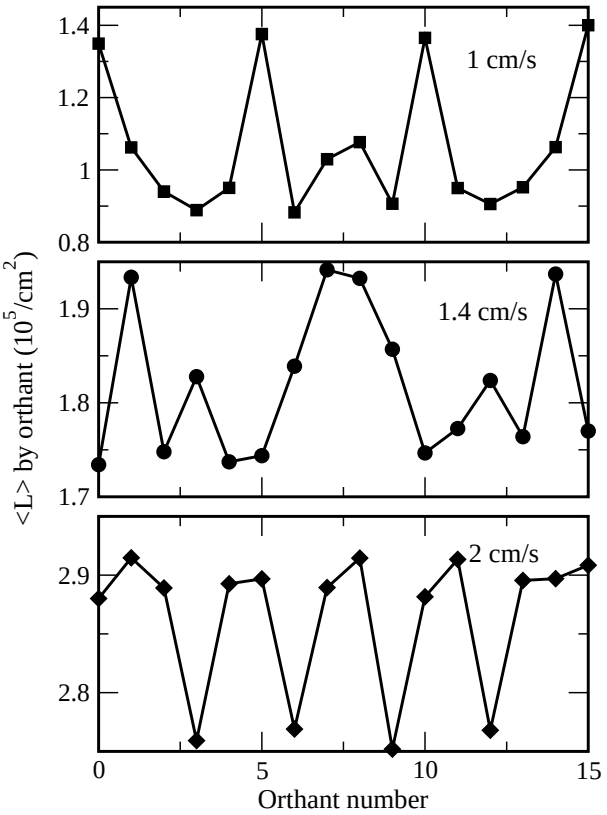


FIG. 8: Line length density for the sixteen orthants of $S^3$, for steady-state tangles with $v_{ns} = 1$ cm/s (top), $v_{ns} = 1.4$ cm/s (center), and $v_{ns} = 2$ cm/s (bottom). In each case the average is over a 4-second interval.

12. These groupings track the velocity field. For example, consider the point $(-\frac{1}{2}, -\frac{1}{2}, -\frac{1}{2}, -\frac{1}{2})$, which lies exactly in the center of orthant 0. The flow line through this point also passes through quadrants 5, 10, and 15; in fact, it reaches the points $(\frac{1}{2}, -\frac{1}{2}, \frac{1}{2}, -\frac{1}{2})$, $(\frac{1}{2}, \frac{1}{2}, \frac{1}{2}, \frac{1}{2})$ and $(-\frac{1}{2}, \frac{1}{2}, -\frac{1}{2}, \frac{1}{2})$ at the centers of these orthants. Likewise the centers of orthants 1, 7, 8, and 14 lie on a common flow line, and similarly for the remaining two sets of orthants. A generic flow line actually passes through *eight* orthants, two of the listed sets of four. The portion of the flow line within an orthant is always identical for the four orthants in a set. In particular, flow lines which pass through a large portion of one orthant do the same for the other orthants in the same group, alternating with briefer sections in the orthants of a second group. Hence it makes sense to think of the velocity field as roughly conveying any vortex tangle from one orthant into the other orthants grouped with it. The implication for homogeneity is that when vortices are swept directly from one orthant to another through the influence of the applied velocity field, the line length in those orthants quickly equilibrates. The process is much slower for orthants in different groups, which do not benefit from this convective mechanism. The resulting lack of global homogeneity for tangles on $S^3$ differs from the situation on $T^3$, where vortex tangles remain homogeneous. As we will see shortly, the reason may be the different anisotropy of tangles in the two spaces.

The same presentation for higher driving velocities appears in the bottom two frames of Figure 8. The same groupings of orthants appear, since that depends solely on the geometry of $S^3$. However, at each velocity different sets of orthants have the largest and smallest line densities. As the velocity increases, the tangle becomes more homogeneous, with variations in $\langle L \rangle$ decreasing in both relative and absolute terms. At $v_{ns} = 2$ cm/s, three sets of orthants have indistinguishable line densities, with the variations among orthants within a set larger than any differences in line density between sets. The fourth set of orthants has a smaller line density than the other three, but only by about 5%.

In simulations on $T^3$, vortices have a slight tendency to align perpendicular to the applied velocity field. We use the anisotropy parameter [7]

$$I_\parallel = \frac{1}{VL} \int [1 - (\hat{\mathbf{s}}' \cdot \hat{\mathbf{r}}_\parallel)^2] d\xi$$

to quantify this effect. Here $\hat{\mathbf{r}}_\parallel$ is a unit vector parallel to the applied flow, $VL$ is the total length of vortices, and the integral is taken over all vortex lines. If the vortices were entirely aligned with the applied velocity field, then $I_\parallel$ would vanish. In the other extreme, with vortices always perpendicular to the applied field, $I_\parallel = 1$. In a perfectly isotopic tangle $I_\parallel = \frac{2}{3}$. Our previous calculations on $T^3$ give $I_\parallel = 0.76$ [18]. Other simulations [7, 9, 13, 19] find similar values for $I_\parallel$ at $\alpha = 0.1$, with a decrease towards 2/3 as $\alpha$ decreases. As shown in Figure 9, the vortex orientation within the 3-sphere tangles is dramatically different. $I_\parallel$ lies between 0.1 and 0.25, depending on the driving velocity. At sufficiently high velocity the anisotropy levels off at about 0.23, implying a significant alignment of vortices with the applied velocity.

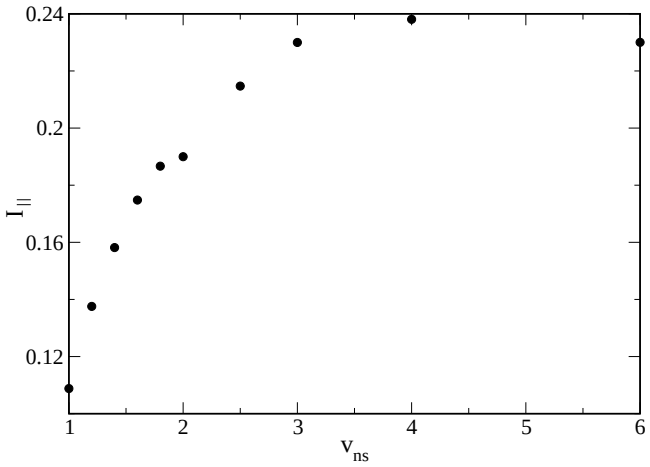


FIG. 9: Anisotropy parameter $I_\parallel$ as a function of applied velocity. For an isotropic tangle, $I_\parallel = 2/3$.

Alignment of vortices along flow lines limits the effectiveness of convection at homogenizing a tangle. Vortices move roughly parallel to their own direction, and the flow

does not force them into interaction with other vortices. By contrast, a vortex locally perpendicular to the velocity field sweeps through a region of space, making vortex crossings more likely. Such a vortex also drags its more distant portions along with it, increasing communication among all parts of the tangle.

The misalignment of the vortices remains large enough to sustain vortex-vortex interactions. Thus polarized turbulence arises naturally on $S^3$ with a Hopf driving field. The structure is entirely different from that of counterflow turbulence on $T^3$, where the polarization is far less and is directed perpendicular to the flow. Anisotropic turbulence in physical experiments can arise from rotation [20], the geometry of the container boundaries, or entrainment by normal fluid turbulence [21]. Boundaries and a turbulent normal fluid are both computationally expensive, but simulations on $S^3$ provide another method of achieving highly polarized turbulence.

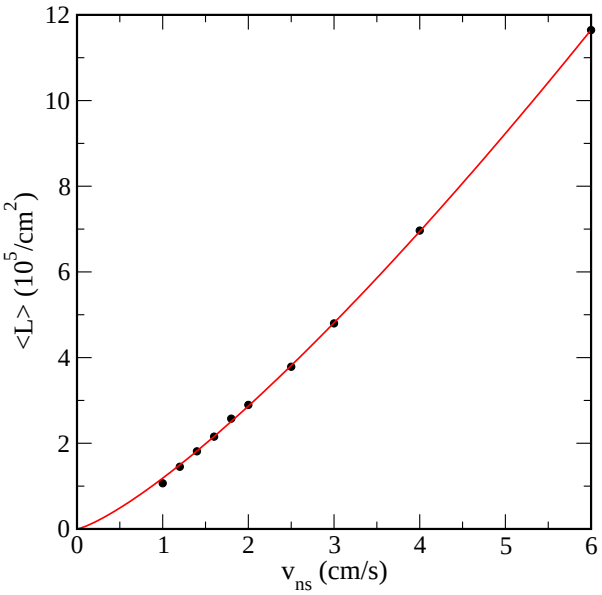


FIG. 10: Line length density as a function of applied velocity. Solid line is a two-parameter fit, yielding $1.19 v_{ns}^{1.28}$, where only velocities $v_{ns} \geq 2$ are used for the fit.

One illustration of the difference between isotropic and anisotropic turbulence is the dependence of the vortex line density on the applied velocity field. Scaling arguments [7, 22] give a clear prediction for isotropic homogeneous tangles: $\beta \langle L \rangle^{1/2}$ should be proportional to $v_{ns}$. This has been observed in experiment [23] and simulations [7, 9, 13]. The scaling breaks down when rotation introduces anisotropy [20, 24]. In these studies the anisotropy parameter changes with $v_{ns}$, obscuring the dependence of $\langle L \rangle$ on $v_{ns}$. For our system, Figure 10 shows the line length after equilibration at each velocity, along with a power-law fit. Rather than finding that $\langle L \rangle$ goes roughly as $v_{ns}^2$, we find an exponent of only 1.28. The reduced exponent is not caused by the lack of global homogeneity. For the fit shown in Figure 10 we use only those trials with velocity at least 2 cm/s, which are nearly homogeneous. Extrapolating the fit curve to lower velocities gives excellent agreement with the line densities found at these low driving velocities, and the fit itself changes little when these points are included. Thus we attribute the change in exponent to the anisotropy of the tangle; certainly anisotropy invalidates the scaling arguments used to derive the quadratic dependence of line density on $v_{ns}$ in isotropic tangles. In fact a reduced exponent makes intuitive sense. Vortices perfectly aligned with the driving velocity cannot gain energy from the applied fields; the $\hat{\mathbf{s}}' \times \mathbf{v_{ns}}$ part of the friction term vanishes. Line length increase can only originate from non-aligned vortices, and since these are underrepresented in our tangles, our line length is less than in the isotropic case.

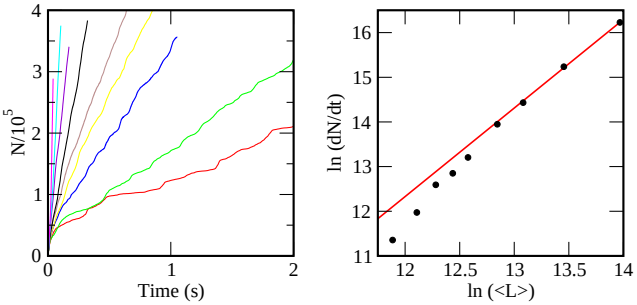


FIG. 11: Left: number of reconnections $N$ as a function of time, for several different velocities. Right: relation between reconnection rate and line length density. Each point corresponds to one of the curves in the left graph, with $dN/dt$ obtained from a linear fit to the long-time part of the $N(t)$ curve. The solid line represents a power-law fit, $dN/dt = c\langle L \rangle^m$, to the highest four points, selected because the corresponding tangles have similar anisotropy. The resulting exponent is $m = 1.98$.

The rate of vortex reconnections can also depend on the structure of the tangle. For isotropic homogeneous turbulence, simple arguments [25, 26] show that the reconnection rate is related to the vortex line density through $dN/dt \propto \langle L \rangle^{5/2}$, which agrees with simulations [19, 25]. Polarization should reduce the number of reconnections [27], since aligned vortices encounter each other less often. Simulations show a reduction of about a factor of two in the number of reconnections in polarized turbulence [28]; here the polarization comes from a normal fluid driving velocity taken from a snapshot of classical turbulence. Polarization is also expected to decrease the scaling exponent. In calculations of counterflow turbulence before the vortex line length stabilized [10], increasing vortex line length produced both an increase in polarization and a decrease in the reconnection rate exponent. Tsubota et al. also found a hint of a reduced exponent [29], albeit without enough data to identify the exponent. In Figure 11 we fit reconnection rate vs. velocity, using only the points corresponding to the four largest driving velocities, where the anisotropy parameter is changing little. We find that the exponent is indeed reduced, to 1.98. The resulting fit does not extrapolate well to the data from lower driving velocity, but that is not surprising since the low-velocity tangles are much more anisotropic, as seen in Figure 9.

Both the average vortex line density and the tangle anisotropy are independent of the initial configuration used. For example, Figure 12 shows that line density for $v_{ns} = 1.4$ cm/s ultimately reaches the same stable level for three initial conditions. The convergence to a common global line density happens despite the inhomogeneity among orthants. This demonstrates that equilibration occurs even with weak direct communication among different parts of the space.

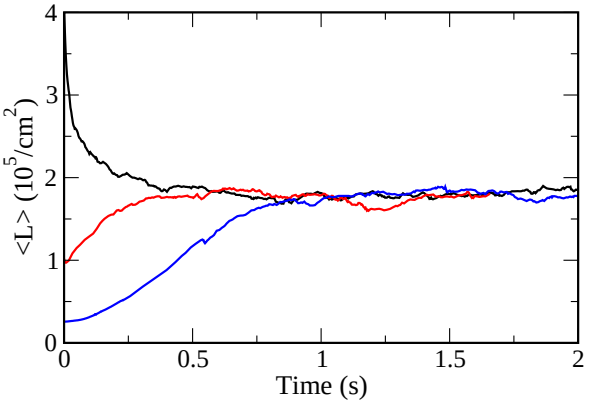


FIG. 12: Line length density as a function of time, for $v_{ns} = 1.4$ cm/s and non-local interactions over the entire volume, for three different initial configurations.

## IV. LOCAL INDUCTION APPROXIMATION

A calculational issue on the 3-torus has been the reliability of the local induction approximation (LIA) that ignores the non-local integral in the equation of motion. Without the non-local term, the tangle can degenerate into an "open-orbit" state, consisting of straight parallel vortex lines that do not interact [7, 8]. Keeping the non-local term solves this problem [9], but given the extra computational demands of the full integral even subsequent work has used LIA [30, 31], compared results from LIA and the full integral [13, 32], or drawn conclusions from prior LIA work [33]. Hence better understanding its limitations remains relevant.

The flow lines of the Hopf field on the 3-sphere do not remain mutually perpendicular throughout the entire space, so we observe nothing directly equivalent to the open-orbit state on the torus. However, omitting the non-local interaction causes a different problem: a collapse of vortex lines until they all lie nearly atop each other. In most cases the vortices in the collapsed state follow roughly along a Hopf fiber, leading to an extremely low anisotropy parameter. Figure 13 illustrates the collapse process at a driving velocity $v_{ns} = 1.4$ cm/s. The first frame shows the anisotropy parameter which initially varies between 0.1 and 0.2, then drops abruptly to about 0.01, with little change thereafter. The remaining frames are Hopf and stereographic projections at three times. The initial configuration is a tangle equilibrated at the same driving velocity but with non-local terms included. As seen from frames d) and e), upon omitting the non-local contributions the vortex line density becomes less uniform, even before any dramatic change in the anisotropy appears. The final frames f) and g) show the complete collapse. Since the Hopf projection sends Hopf fibers to points, the small size of the ring in f) indicates that the vortices stray little from a single Hopf fiber. In frames f) and g) there are three distinct vortices present, which make a combined total of seven circuits. Continuing the calculation leads to trivial reconnections among these near-parallel vortices, but no other interactions occur and the collapsed state persists indefinitely.

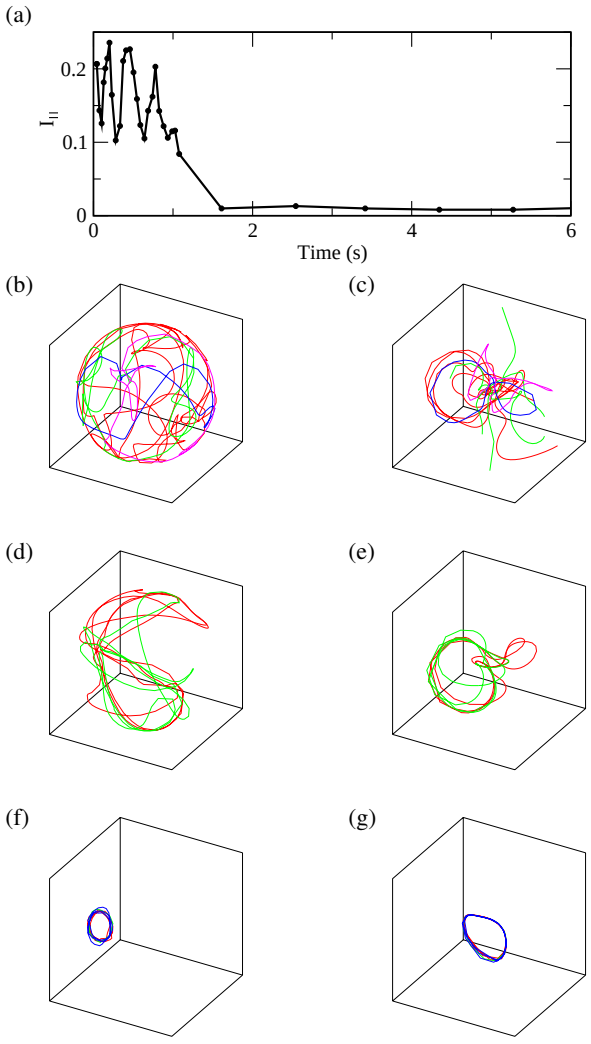


FIG. 13: Development of vortices for $v_{ns} = 1.4$ cm/s, with no non-local contribution. Frame a shows the anisotropy density as a function of time. Frames b, d, and f are Hopf projections of the vortices at $t = 0$, 0.5, and 1.6 s, all with the same scale. Frames c, e, and g are stereographic projections at the same times, again all with the same scale.

Low-velocity calculations without the non-local contribution routinely collapse to a set of nearly-overlapping loops, composing one or more vortex rings. While the loops are usu-

ally close to a Hopf fiber, with anisotropy parameter $I_{\|} < 0.02$, that is not always the case. One of our collapsed configurations had final anisotropy parameter an order of magnitude larger, $I_{\|} = 0.27$. For our usual right-handed Hopf flow, the vortex loop is roughly aligned with the flow. Starting with what appears to be a stable configuration and inverting the direction of all vortices causes immediate vortex motion, as the loops rotate by $\pi$ relative to the Hopf flow. Similarly, for a left-handed Hopf flow stable vortices are anti-parallel to the field. This direction change is exactly as expected since vortices are axial vectors. Oddly, the persistence of such vortex arrangements depends on having several loops; upon removing all but a single loop, that loop moves and distorts until eventually additional loops are created. The requirement of multiple loops is particularly strange given that the LIA calculation does not include non-local interactions, so the loops interact solely through reconnections. The collapsed state appears to be a numerical artifact specific to using the local approximation on $S^3$, much as the open-orbit state is on $T^3$.

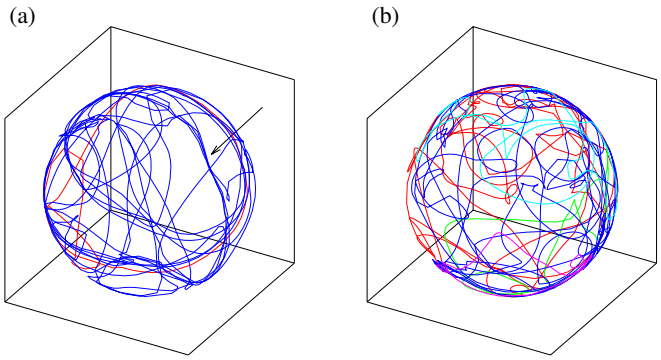


FIG. 14: Hopf projections for tangles generated with no non-local contributions (a) and with non-local contributions included out to a distance $d_{NL} = 0.1\pi R$ (b). For both tangles $v_{ns} = 2$ cm/s and the sphere radius is $r = 0.005$ cm. Vortex clustering appears in (a), as indicated by the arrow, but is mostly eliminated in (b) by the short-distance non-local contributions.

For sufficiently large driving velocity, a non-trivial vortex tangle persists even without non-local contributions, as illustrated in Figure 14a. However, hints of the collapsed state remain, in the tendency of vortices to clump together. Without the non-local term to separate them, portions of vortices that become aligned will continue their time development together until disrupted by reconnection with a non-aligned vortex. As with the open-orbit state on $T^3$, adding non-local contributions out to a very limited distance disrupts the collapsed state. The tangle of Figure 14b, which results from including contributions out to a distance $d_{NL} = 0.1\pi R$, shows little sign of the clustering that results from the purely local calculation. Our calculations suggest that with non-local terms included even for such a small fraction of the sphere, the tangles can persist indefinitely.

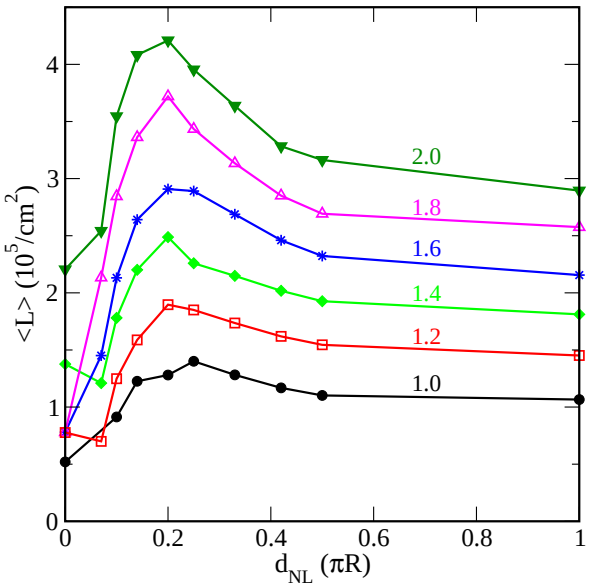


FIG. 15: Equilibrated line length density as a function of the extent of the non-local calculation, for several applied velocity fields. The velocities, in cm/s, are indicated above each curve.

## V. EFFECT OF NON-LOCAL TERM

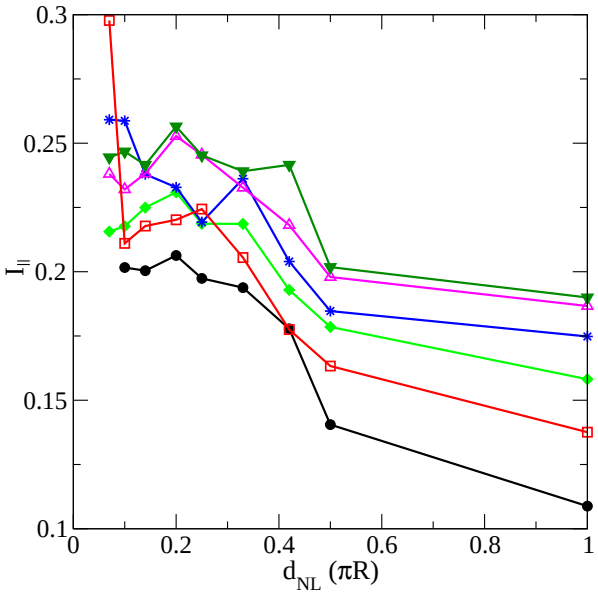


FIG. 16: Anisotropy parameter as a function of the extent of the non-local calculation, for several applied velocities. The driving velocities, in cm/s, are 1.0, 1.2, 1.4, 1.6, 1.8, and 2.0, with $I_{\|}$ strictly increasing with drive at $d_{NL} = 1$.

As with our previous simulations with the usual periodic boundary conditions [18], we examine the effects of including non-local terms only for vortices within a distance $d_{NL}$. Figure 15 shows the results. At very small $d_{NL}$, the main ef-

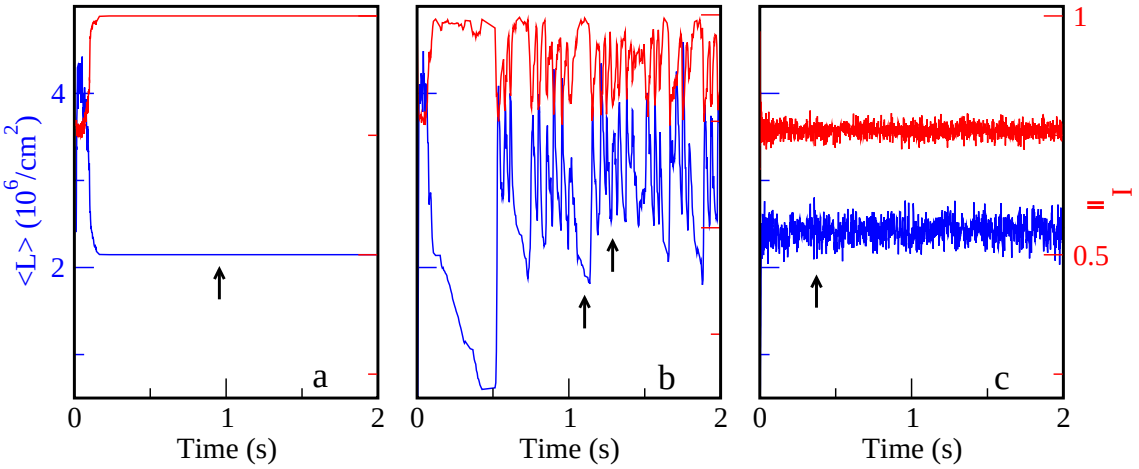


FIG. 17: Line length density (lower curves, left axes) and anisotropy (upper curves, right axes) on a torus, with $v_{ns} = 12$ cm/s. a) LIA only, straight velocity field, b) LIA only, helical velocity field, c) full Biot-Savart law, straight velocity field. Arrows indicate the configurations shown in Figure 18.

fect is to dissipate the clumping, since intervortex interactions separate the vortex lines. Forcing the vortices apart also helps to maintain a true tangle. Without the non-local interaction, the vortices can collapse along a flow line, which prevents further energy gain or loss in the tangle. The non-local term and resulting reconnections ensures that some of the vortex loops have segments perpendicular to the velocity field. These perpendicular segments exchange energy with the applied field, allowing the line density to grow. As $d_{NL}$ increases further, the line length density of the tangle decreases gradually. This is analogous to our previous results for periodic boundary conditions, where the non-local interaction reduces the line length by favoring reconnections between anti-parallel vortices over those between near-parallel vortices. However, with periodic boundary conditions this decrease in $\langle L \rangle$ occurs mainly when $d_{NL}$ is smaller than the typical vortex separation. At larger $d_{NL}$ the line length is nearly constant. Effectively, only "nearest-neighbor" vortices contribute significantly to the velocity field. The much more gradual effect of non-local terms in $S^3$ may arise from the anisotropic nature of the tangles, which means that distant non-local contributions are not directed randomly and do not cancel as efficiently as they do on the torus. Interestingly, the crossover between the low-$d_{NL}$ reduction of clumping and the high-$d_{NL}$ reduction of line length occurs when the non-local term is applied over a distance comparable to the vortex line spacing. In fact, the maximum line length density seems to move towards smaller $d_{NL}$ as the applied velocity field increases, consistent with the reduced line spacing at higher velocities.

As shown in Figure 16, the tangles become slightly more anisotropic as the driving velocity decreases, probably because at lower line density there are fewer reconnections. The anisotropy is relatively constant at low $d_{NL}$, but increases as the interactions extend beyond one hemisphere. This increased anisotropy is entirely different from the collapse observed as $d_{NL} \to 0$, and much more subtle. The vortices remain intertwined, but with an incomplete tendency to align with the velocity field. The increase in this alignment when the interactions reach a full hemisphere suggests that the coupling of distant regions through the full $S^3$ Biot-Savart law plays a significant role in the anisotropy. In fact, extending the interactions from one hemisphere to the entire sphere affects the anisotropy more than it does the line density. Figure 16 omits combinations of $d_{NL}$ and $v_{ns}$ for which the tangle collapses to a single trajectory of nearly overlapping vortices. At the lowest $d_{NL}$ where the vortices do not completely collapse, $I_{\|}$ relies heavily on a small number of vortex loops and becomes erratic, for example at $v_{ns} = 1.2$ cm/s and $d_{NL} = 0.07\pi R$.

## VI. POLARIZATION OF TANGLES

We now return to the significant difference in tangle anisotropy between simulations on $T^3$ and $S^3$. In the torus calculations with periodic boundary conditions we find a slight tendency of vortices to align perpendicular to the driving velocity field. The Glaberson-Donnelly instability [34], which has been observed by various groups both experimentally [20, 35] and in computational work [24, 36], prevents parallel alignment. Essentially, for a straight vortex parallel to an external velocity field, certain distortions of the vortex away from straight tend to grow. With multiple vortices, such growth ultimately leads to reconnections that alter the vortex arrangement. The Glaberson-Donnelly instability also impacts simulations using the local induction approximation, where an "open-orbit" state appears with non-interacting vortices aligned in a single direction. The vortex direction is always perpendicular to the driving velocity because of the instability.

By contrast, on $S^3$ the driving velocity field follows helical Hopf fibers. This means that no set of parallel vortices, all perpendicular to the velocity field throughout the 3-sphere, can exist. Another factor weakening the Glaberson-Donnelly

instability is that, unlike on the torus, the longest-wavelength distortion of a flow line is itself another flow line. This holds only for a distortion with handedness matching that of the Hopf flow, which is consistent with our observation that vortex rings can only settle stably in one direction relative to the Hopf flow. For LIA calculations we find near-perfect alignment with the Hopf field. The polarization drops once non-local interactions are included, although the turbulence remains anisotropic with a tendency towards parallel alignment.

This raises the question of whether a helical velocity field on a torus would lead to some of the same behavior as the Hopf flow on the 3-sphere. We carried out a few such simulations, using a helical field around the $z$-axis. The field makes three rotations and has horizontal magnitude 10% of the total. The helical field indeed prevents the full open-orbit state from developing even when using the local induction approximation. However, the vortex line density still differs from that of the full non-local calculation. Figure 17 shows the relatively stable line density from a full non-local calculation, along with the perfectly stable line density from LIA once the open orbit state has formed. The exact open-orbit line density varies depending on the initial conditions; in this case it is slightly lower than that of the non-local calculation. The helical velocity field leads to entirely different behavior. The tangle undergoes frequent excursions towards the open-orbit state, with the anisotropy coefficient becoming very large; Figure 18c illustrates a configuration with $I_{\|} = 0.992$ and $\langle L \rangle = 1.9 \times 10^6/\mathrm{cm}^2$. Unlike in the complete open-orbit state of Figure 18a, slight curvature and misalignment remain. Remarkably, the helical velocity field enables recovery even from such a well-aligned configuration. A short time later, the vortices reach the configuration of Figure 18d, with $I_{\|} = 0.787$ and $\langle L \rangle = 3.4 \times 10^6/\mathrm{cm}^2$. The tangle remains noticeably less homogeneous than that of Figure 18b, which comes from a fully non-local calculation and has $I_{\|} = 0.787$ and $\langle L \rangle = 2.6 \times 10^6/\mathrm{cm}^2$. Figure 17b shows repeated fluctuations between these limits. The dependence on the helicity of the applied velocity field is entirely an effect of LIA; a full non-local calculation with helical applied velocity has density and anisotropy unchanged form Figure 17c.

## VII. CONCLUSIONS

We have carried out vortex simulations on a 3-sphere. Our results show the potential importance of the global geometry and topology used. The most basic features remain the same as in standard torus-based calculations. Vortex tangles appear, with the vortex line length stabilizing at a value that increases with the driving velocity. However, the tangles are much less isotropic than those generated on a torus. Exponents relating the line length to the driving velocity and the reconnection rate reflect this increased anisotropy. This suggests the intriguing possibility of generating steady-state tangles with markedly different properties by changing the underlying global structure. More broadly, computations throughout condensed matter are done on a torus, often without investigating what features may stem from the topology itself.

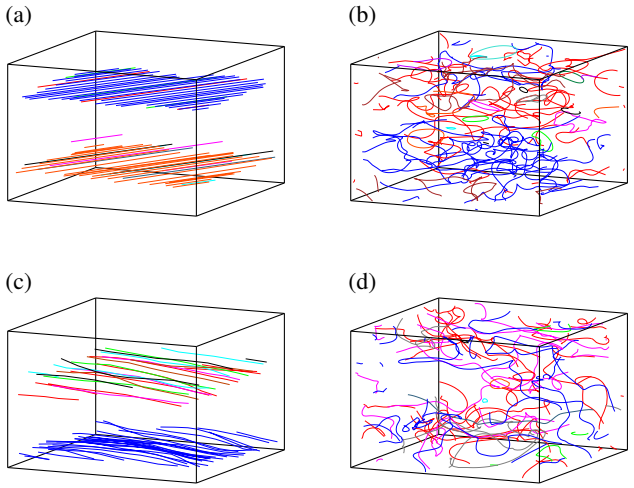


FIG. 18: Vortex configurations for torus simulations, corresponding to the points noted in Figure 17. a) LIA only, straight velocity field, b) full Biot-Savart law, c) LIA only, helical velocity field, high anisotropy, d) LIA only, helical velocity field, low anisotropy.

In calculations using the local induction approximation, the influence of the manifold was even more striking. The particular failure mode on $T^3$, the open orbit state, did not appear, but vortices instead collapsed to occupy a thin tube, all with nearly parallel alignment. A helical driving velocity on $T^3$, which shares some properties with the flow on $S^3$, avoids the full open orbit state under LIA but retains much of the same character. This is further evidence of the role of the manifold rather than the specific velocity field.

## ACKNOWLEDGMENTS

We thank G. Kuperberg for many helpful conversations, including bring to our attention the exact Biot-Savart formula on $S^3$. One of us (Dix) acknowledges funding from a Department of Education GAANN fellowship.

## APPENDIX

*Stereographic Projection*

In this case $S^3$ is mapped onto $\mathbb{R}^3$. Figure 19 shows the analogous operation mapping $S^2$ to the $z = 0$ plane. The projection point $p$ is (0,0,$R$). A line is extended from $p$ through a point on the circle, and the intersection between that line and the $xy$-plane gives the image point. Under this projection, the equator maps to a circle of radius $R$. The lower hemisphere goes to the inside of this circle, and the outer hemisphere to the outside. The projection point itself does not have an image within the plane, but maps to a point at infinity. In general, the image of a point $(x, y, z)$ in $S^2$ has coordinates

$$\left(\frac{x}{1 - z/R}, \frac{y}{1 - z/R}\right)$$

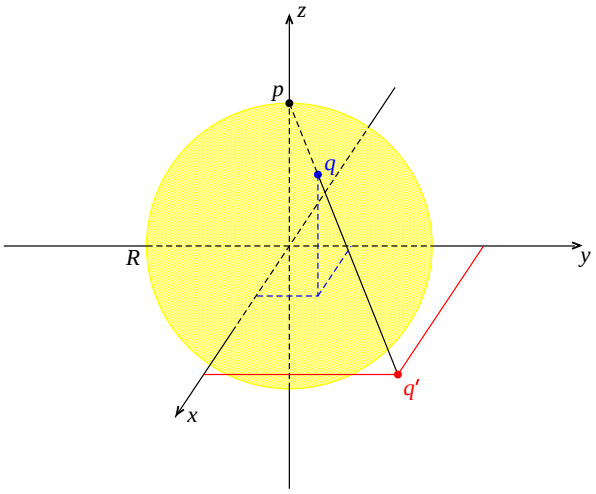


FIG. 19: Illustration of stereographic projection from the surface of a three-dimensional ball to the $xy$ plane. A point $q$ maps to $q'$ in the plane such that $q$, $q'$, and $p$ are collinear.

in the plane. The generalization to a projection from $S^3$ to, say, the $w = 0$ space is straightforward.

The main disadvantage of stereographic projection is that distances are not preserved. One half of $S^3$ maps to the inside of a finite sphere, while the other half maps to the infinite outside. This can give a misleading impression of the structure of a vortex tangle.

*Hopf Fibration*

A Hopf fibration maps $S^3$ onto $S^2$ in a way that preserves distance, up to an overall scale factor. It is selected to match our driving velocity field, $\mathbf{v} = \frac{v}{R}(-y, x, -w, z)$; as we show below, the corresponding Hopf fibration maps each flow line to a single point. We take the Hopf fibration as the following map to $\mathbb{R}^3$:

$$\begin{aligned} h_1 &= 2(xz + yw) \\ h_2 &= 2(yz - xw) \\ h_3 &= (x^2 + y^2) - (z^2 + w^2) \end{aligned}$$

Explicit multiplication shows that for any point on a 3-sphere of radius $R$, its image is at radius $R^2$. Thus $S^3$ in fact maps to $S^2$.

The flow lines of the velocity field are particular great circles on $S^3$. To track them under the Hopf fibration, consider the four-dimensional real space which contains $S^3$ as a two-dimensional complex space with coordinates $q_1 = x + iy$ and $q_2 = z + iw$. A complex line, $q_2 = kq_1$, intersects $S^3$ in a great circle of constant $|q_1|$ and $|q_2|$, which is exactly a flow line of this velocity field. In addition, writing the Hopf fibration in terms of the complex coordinates and using $q_2 = kq_1$ gives

$$\begin{aligned} h_1 &= Re(2q_1 q_2^*) = 2|q_1|^2 Re(k) \\ h_2 &= Im(2q_1 q_2^*) = 2|q_1|^2 Im(k) \\ h_3 &= |q_1|^2 - |q_2|^2 = |q_1|^2(1 - |k|^2) \end{aligned}$$

The image depends only on $k$ and $|q_1|$, both of which are constant on any great circle corresponding to a flow line of the velocity field. Hence this Hopf fibration maps a flow line on $S^3$ to a point on $S^2$.

Any two Hopf fibers of the flow are great circles that twist around each other. The distance between any point on one fiber and the closest point on the other is constant, which gives a sensible definition for the distance between the two fibers. The Hopf fibration preserves this distance, up to an overall scale factor. For example all fibers a fixed distance from a given fiber $A$ are mapped to a circle on $S^2$ centered at the image of $A$.


[1] J. Blazek, *Computational Fluid Dynamics, Principles and Applications*, Third Edition (Elsevier Ltd., Amsterdam, 2015).

[2] M. Maxey, "Simulation Methods for Particulate Flows and Concentrated Suspensions," *Ann. Rev. Fluid Mech.* **49**, 171 (2017).

[3] M.L. Hosain and R.B. Fdhila, "Literature Review of Accelerated CFD Simulation Methods towards Online Application," *Energy Procedia* **75**, 3307 (2015).

[4] G.-H. Cottet and P.D. Koumoutsakos, *Vortex Methods: Theory and Practice* (Cambridge University Press, Cambridge, 2000).

[5] K.W. Schwarz, "Three-Dimensional Vortex Dynamics in Superfluid $^4$He: Line-Line and Line-Boundary Interactions," *Phys. Rev. B* **31**, 5782 (1985).

[6] M. Tsubota, K. Fujimoto, and S. Yui, "Numerical Studies of Quantum Turbulence," *J. Low Temp. Phys.* **188**, 119 (2017) and arXiv:1704.02566.

[7] K.W. Schwarz, "Three-Dimensional Vortex Dynamics in Superfluid $^4$He: Homogeneous Superfluid Turbulence," *Phys. Rev. B* **38**, 2398 (1988).

[8] R.G.M. Aarts, *A Numerical Study of Quantized Vortices in HeII*, Ph.D. thesis, Eindhoven University of Technology (1993).

[9] H. Adachi, S. Fujiyama, and M. Tsubota, "Steady-State Counterflow Quantum Turbulence: Simulation of Vortex Filaments using the Full Biot-Savart Law," *Phys. Rev. B* **81**, 104511 (2010) and arXiv:0912.4822.

[10] C. Barenghi and D. Samuels, "Scaling Laws of Vortex Reconnections," *J. Low Temp. Phys.* **136**, 281 (2004).

[11] V.I. Arnold and B.A. Khesin, *Topological Methods in Hydrodynamics* (Springer-Verlag, New York, 1998), p. 127.

[12] M.P. do Carmo, *Differential Geometry of Curves and Surfaces* (Prentice-Hall, Englewood Cliffs, 1976).

[13] L. Kondaurova, V. L'vov, A. Pomyalov, and I. Procaccia, "Structure of a Quantum Vortex Tangle in $^4$He Counterflow Turbulence," *Phys. Rev. B* **89**, 014502 (2014) and arXiv:1306.6167.

[14] D. DeTurck and H. Gluck, "Electrodynamics and the Gauss Linking Integral on the 3-Sphere and in Hyperbolic 3-Space," *J. Math. Phys.* **49**, 023504 (2005) and arXiv:math/0510388.

[15] G. Kuperberg, "From the Mahler Conjecture to Gauss Linking Integrals," *Geom. Funct. Anal.* **18**, 870 (2008) and arXiv:math/0610904.

[16] W.P. Thurston, *Three-Dimensional Geometry and Topology*

(Princeton University Press, Princeton, 1997).

[17] A.W. Baggaley and C.F. Barenghi, "Tree Method for Quantum Vortex Dynamics," *J. Low Temp. Phys.* **166**, 3 (2012) and arXiv:1108.1119.

[18] O.M. Dix and R.J. Zieve, "Nonlocality in Homogeneous Superfluid Turbulence," *Phys. Rev. B* **90**, 144511 (2014) and arXiv:cond-mat/1309.1797.

[19] M. Tsubota, T. Araki, and S. Nemirovskii, "Dynamics of Vortex Tangle without Mutual Friction in Superfluid $^4$He," *Phys. Rev. B* **62**, 11751 (2000) and arXiv:cond-mat/0005280.

[20] C.E. Swanson, C.F. Barenghi, and R.J. Donnelly, "Rotation of a Tangle of Quantized Vortex Lines in He II," *Phys. Rev. Lett.* **50**, 190 (1983).

[21] C.F. Barenghi, S. Hulton, and D.C. Samuels, "Polarization of Superfluid Turbulence," *Phys. Rev. Lett.* **89**, 275301 (2002) and arXiv:cond-mat/0208135.

[22] C.E. Swanson and R.J. Donnelly, "Vortex Dynamics and Scaling in Turbulent Counterflowing Helium II," *J. Low Temp. Phys.* **61**, 363 (1985).

[23] K.P. Martin and J.T. Tough, "Evolution of Superfluid Turbulence in Thermal Counterflow," *Phys. Rev. B* **27**,2788 (1983).

[24] M. Tsubota, T. Araki, and C.F. Barenghi, "Rotating Superfluid Turbulence," *Phys. Rev. Lett.* **90**, 205301 (2003) and arXiv:cond-mat/0301412.

[25] D.R. Poole, H. Scoffield, C.F. Barenghi, and D.C. Samuels, "Geometry and Topology of Superfluid Turbulence," *J. Low Temp. Phys.* **132**, 97 (2003).

[26] S. Nemirovskii, "Evolution of a Network of Vortex Loops in He-II: Exact Solution of the Rate Equation," *Phys. Rev. Lett.* **96**, 015301 (2006) and arXiv:cond-mat/0505742.

[27] V.S. L'vov, S.V. Nazarenko, and O. Rudenko, "Bottleneck Crossover Between Classical and Quantum Superfluid Turbulence," *Phys. Rev. B* **76**, 024520 (2007); arXiv:nlin/0612018.

[28] J. Laurie and A.W. Baggaley, "Reconnection Dynamics and Mutual Friction in Quantum Turbulence," *J. Low Temp. Phys.* **180**, 82 (2015) and arXiv:1410.2515.

[29] M. Tsubota, C.F. Barenghi, T. Araki, and A. Mitani, "Instability of Vortex Array and Transitions to Turbulence in Rotating Helium II," *Phys. Rev. B* **69**, 134515 (2004) and arXivz;cond-mat/0305578.

[30] H. Salman, "Breathers on Quantized Superfluid Vortices," *Phys. Rev. Lett.* **111** 165301 (2013) and arXiv:1307.7531.

[31] R.A. Van Gorder, "Motion of a Helical Vortex Filament in Superfluid $^4$He Under the Extrinsic Form of the Local Induction Approximation," *Phys. Fluids* **25**, 085101 (2013).

[32] J. Laurie and A.W. Baggaley, "A Note on the Propagation of Quantized Vortex Rings Through a Quantum Turbulence Tangle: Energy Transport or Energy Dissipation?" *J. Low Temp. Phys.* **180**, 95 (2015); arXiv:1410.2525.

[33] S.K. Nemirovskii, "Statistical Signature of Vortex Filaments in Classical Turbulence: Dog or Tail?" arXiv:1902.06214.

[34] W.I. Glaberson, W.W. Johnson, and R.M. Ostermeier, "Instability of a Vortex Array in He II," *Phys. Rev. Lett.* **33**, 1197 (1974).

[35] D.K. Cheng, M.W. Cromar, and R.J. Donnelly, "Influence of an Axial Heat Current on Negative-Ion Trapping in Rotating Helium II," *Phys. Rev. Lett.* **31**, 433 (1973).

[36] M. Mesgarnezhad, R.G. Cooper, A.W. Baggaley, and C.F. Barenghi, "Helicity and Topology of a Small Region of Quantum Vorticity," *Fluid Dyn. Res.* **50**, 011403 (2018).